Nanoscale

PAPER

View Article Online
View Journal | View Issue

Cite this: *Nanoscale*, 2025, **17**, 5798

Water oxidation on a sustainable polymeric proton relay: the role of post-phosphating of an oxide sub-layer on PCET†

Kimia Ahanjan, Mojtaba Shamsipur * and Afshin Pashabadi *

Received 26th October 2024,
Accepted 23rd January 2025

DOI: 10.1039/d4nr04386c

rsc.li/nanoscale

Lagging proton transfer (PT) toward electron transfer (ET) during multi-step proton-coupled electron transfer (PCET) is one of the humble approaches toward complete biomimicking of artificial leaves. In this work, we synthesized a typical sustainable polymeric interface (poly L-lysine) to investigate the effect of post-phosphating of the metal oxide substrate (NF/$CoMoO_4$) on the yield of PCET during the electrocatalytic water oxidation reaction (WOR) in alkaline medium. The details of the PCET mechanism are unraveled using the kinetic isotope effect (KIE), proton inventory, Tafel slopes, pH studies, and high-frequency transmission line (Gerischer) impedance. The appealing Gerischer feature unveils an electrochemical reaction preceded and followed by a chemical exchange reaction (CEC mechanism), indicating a proton hopping mechanism that practically blocks natural diffusion of the protonic species (H^+ and H_2O) and the role of the interfacial phosphate#p-Lys hydrogen bond network (HBN) in PCET. The interfacial HBN can serve as a flexible proton hook to delocalize protons and may polarize the O–O bond, thereby facilitating the overall PCET for the progress of O–O bond formation. Poly L-lysine improved the response stability of the PCET catalyst through corrosion protection of the metallic substrate and also prevention of the spatiotemporal accumulation of protons as a surface corrosion agent. The results show a non-concerted PCET mechanism with the first ET step as the RDS of the heterogeneous WOR.

Introduction

The sluggish concurrent movement of four electrons and protons in the anodic portion, the water oxidation reaction (WOR), limits the yield of artificial water splitting.[1–3] Depending on the propulsion force (PT or ET) of proton-coupled electron transfer (PCET), the WOR may proceed through either concerted or non-concerted (stepwise) approaches respectively in electrocatalysts or proton relays. PCET possesses a energetic advantage over pure ET due to the attraction between negative electrons and positive protons, which leads to the electrostatic stabilization of the system.[4] During the electrocatalytic WOR, lagging sluggish PT against ET, because a proton/electron mass ratio of 1837, mandates using a solution base (OH^-) that acts as a proton snatcher.[5,6] However, the process is impeded by the limited kinetics of diffusion within the diffusion layer, and the transmutation and the instability of the electrocatalyst body in harsh medium.

During the natural WOR performed in the core of photosystem II (PSII), a five S-state catalytic loop is completed by shuttling of protonic species through intricate hydrogen bond networks (HBNs) of the water–amino acid channels.[3,7,8] The lagging two-way route of substrate delivery (water molecules) and proton excretion in the channels results in an incomplete WOR and the creation of harmful reactive oxygen species like $OH^\bullet$, which can damage the Mn cubane ($CaMn_4O_5$) active core.[9] The deprotonation process and circumvention of charge accumulation permit reaching high oxidation states within a narrow potential range and facilitate the catalytic reaction. Learning from HBNs positioned around $CaMn_4O_5$ guides in creating a holistic blueprint for establishing biomimetic artificial leaves.[3,9,10] In PSII, profiting from a Grotthuss-like mechanism, the protons liberated from the catalytic loop with different S-states are excreted rapidly through HBN channels positioned from $CaMn_4O_5$ to the lumenal bulk.[11,12] HBNs with simple functionality may limit one of the H^+ or H_2O shuttling processes.[13] Theoretically, the water chain enclosed by H-bond acceptors like C═O or P═O can just transport protons. Meanwhile, the H-bond donor's residues like N–H may only transport H_2O.[13] Therefore, compliance with the blueprint concerning the diversity of functions in the design of interfacial proton relay is beneficial for boosting overall PCET. Our

---

Department of Chemistry, Razi University, Kermanshah, Iran.
E-mail: apashabadi@razi.ac.ir

† Electronic supplementary information (ESI) available. See DOI: **https://doi.org/10.1039/d4nr04386c**

research groups recently studied the mechanistic aspects of different inorganic and organic proton relays with identical functionality.[5,6,9,14] The function diversity of HBNs in the interfacial proton relay serves an increased rigidity, intensifies the proton orientation (prevents proton wondering) of water molecules in a fixed scaffold and facilitates proton transfer *via* the Grotthuss-like process.[13]

In neutral and basic solutions, the phosphate ion, as an appealing additional proton acceptor, has been explored in addition to the hydroxyl proton acceptor.[15,16] However, the kinetics of the heterogeneous WOR are limited by the inherent issue of the slow diffusion of the homogeneous proton acceptors. Therefore, combining surface-confined organic proton relays with anchoring proton acceptors, such as phosphates, to enhance the interfacial PT is a potential approach. The phosphate group as a well-known nucleophile and proton acceptor, which directly influences the long-term stability of catalysts, has recently been applied as a modifier of inorganic oxide-based oxygen evolution reaction (OER) catalysts.[17]

Metal molybdates like $MnMoO_4$, $NiMoO_4$, and $CoMoO_4$ have been extensively studied for sustainable energy and catalysis.[18–20] Among them, $CoMoO_4$ stands out by combining cobalt oxide's robust electrochemical activity with molybdenum oxide's diverse polymorphic characteristics to mediate multiple redox reactions.[21] However, their poor electrical conductivity and low interfacial activity in PCET can be improved through surface modification with inorganic donor/acceptor residues like phosphate groups, which are capable of bond bridging and nucleophile activation when attacking the substrate water molecules. Few previous studies have considered the stability of intermediates through H-bonding and the kinetic control of PCET during the heterogeneous WOR.[5,6,14,22–24]

In this study, we examined the pendant amine group's (p-Lys) capacity to function as a polymeric proton relay in the WOR. We fabricated a nickel foam/cobalt molybdenum oxide ($CoMoO_4$) as a typical catalytic substrate for electron transport. Furthermore, hydrothermal phosphating of the substrate (as CoMoP) has been targeted to explore the possible contribution of phosphate groups in PCET and translocation of the liberated protons through bond bridging between the chemisorbed protonic species (–OH* and –OOH*) and the interfacial amine-phosphate HBN. The results of proteo/deutero isotopic studies unravel the superior performance of CoMoP/p-lysine that gets a lower kinetic isotopic effect (KIE) value toward $CoMoO_4$/p-Lys. To extract sufficient mechanistic information, we also performed additional experimental studies including D/H kinetic proton inventory, pH dependency on the RHE scale, Tafel slopes, atom proton transfer (APT), and Gerischer impedance spectroscopy (GIS). Using pH and GIS studies, we suggested a non-concerted PCET and a chemical–electrochemical–chemical (CEC) mechanism. The change of the PCET mechanism from a concerted mechanism on the metallic substrate to a non-concerted mechanism on CoMoP/p-lysine unravels the direct and profound contribution of proton relay in PCET occurring at the electrode/electrolyte interface. The CEC mechanism supports the efficient proton hopping mechanism so that the natural diffusion of protonic species is blocked. The proposed mechanism describing the transition state is a wedge mechanism found in an H-bond complex that emerges as an intermediate in the PT with augmented stability in H-bonding in the transition state of PCET. The as-prepared electrode exhibited an excellent catalytic performance with an overpotential as low as 230 mV to reach a current density (J) of 10 mA cm^{-2} and an onset potential of 1.43 *vs.* reversible hydrogen electrode (RHE) in 1.0 M KOH.

Results and discussion

Characterization

Cobalt/molybdenum oxide (NF/$CoMoO_4$) was synthesized *via* hydrothermal processes and subsequently subjected to post-phosphating treatments, resulting in the formation of NF/CoMoP. To investigate the influence of a metallic substrate on the functionality of p-lysine as a potential polymeric proton relay, a series of metal-supported PCET catalysts, namely NF/p-lysine, NF/$CoMoO_4$/p-lysine, and NF/CoMoP/p-lysine, were fabricated through electropolymerization of the L-lysine monomer (the synthesis details are provided in the ESI†). NF/$CoMoO_4$, NF/$CoMoO_4$/p-Lys, NF/CoMoP, NF/p-Lys, and NF/CoMoP/p-Lys were characterized using elemental mapping and SEM studies (Fig. 1A–E). A dense, rectangle, and cube-like morphology $CoMoO_4$ with an average diameter of 200 nm was produced on NF through a hydrothermal procedure (Fig. 1A). Fig. 1B shows the SEM image of p-lysine electrochemically polymerized on NF/$CoMoO_4$. The EDXA/elemental mappings of the NF/$CoMoO_4$ and NF/$CoMoO_4$/p-lysine electrodes (Fig. S1 and S2†) exhibit the uniform distribution of Co, Mo, O, C, and N on the electrode surface. In Fig. 1C, the SEM images show a striking urchin-like morphology of the NF/CoMoP electrode, (the corresponding EDXA profiles are shown in Fig. S3†). The phosphating of $CoMoO_4$ micro-nanostructures is accomplished by a simple post-hydrothermal process using $Na_2H_2PO_4$ as a phosphating reagent, which leads to a change in the rectangle cube-like morphology to the urchin-like morphology and a reduction in the micro-nanostructure's thickness, exposing more active sites and boosting electrochemical activities.[22] Fig. 1D depicts the SEM image of NF/p-Lys with a stack morphology formed on the NF. Fig. 1E shows the SEM image and corresponding elemental mapping of the electropolymerized p-lysine on NF/CoMoP, a stacked polymer on the urchin-like CoMoP. Fig. S1–S4† in the ESI demonstrate further comparable mapping analyses and EDXA profiles. Fig. 1F shows the corresponding Raman spectra of NF/p-lys from 100 to 3000 cm^{-1}. The bands between 1300 and 1500 cm^{-1} are due to the symmetric carboxylate stretching mode, while the bands between 800 and 1000 cm^{-1} are attributed to the C–COO and C–OH stretching modes. Several additional bands found at 1678 and 1240 cm^{-1} are assigned to the amide I and amide III modes, respectively, which were already observed at similar Raman shifts in the Raman spectrum of p-lys.[25,26]

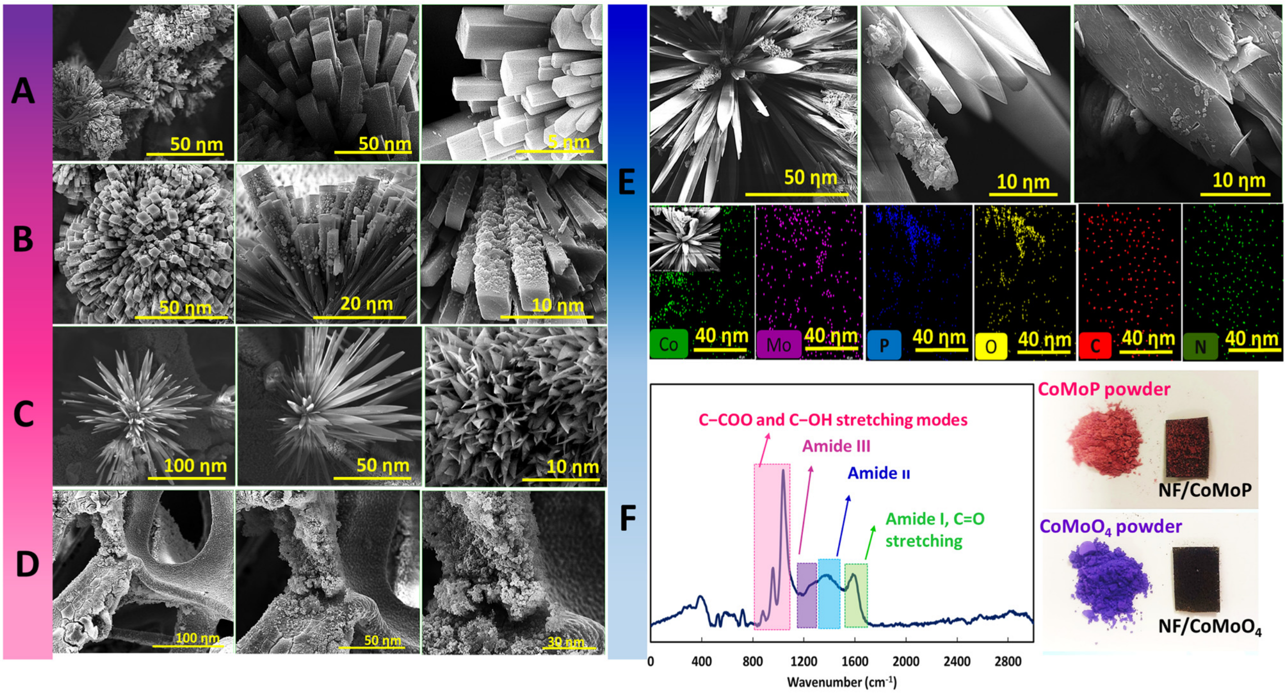

Fig. 1 Typical SEM images of (A) NF/$CoMoO_4$, (B) NF/$CoMoO_4$/p-lysine, (C) NF/CoMoP, and (D) NF/p-lysine. (E) Typical SEM images and the corresponding elemental mapping images of the selected area of the NF/CoMoP/p-lysine electrode. (F) Raman spectra obtained for the NF/p-lys electrode (left). Digital images of the synthesized powders (collected from the bottom of the Teflon autoclave) and the corresponding electrodes (right).

XPS and XRD studies

Low-resolution X-ray photoelectron spectroscopy (XPS) was utilized to evaluate the surface composition and oxidation states of the CoMoP powder sample collected from the Teflon vessel bottom. The result indicates the presence of Co 2p, Mo 3d, P 2p, and O 1s peaks (Fig. 2A). Fig. 2B displays a high-resolution Co 2p spectrum with two main peaks, Co 2p1/2 and Co 2p3/2, revealing 2+ oxidation state of cobalt. Satellite peaks at higher binding energies are observed at 795, 798.3, 812, and 802.7 eV.[27] The spectral region of the Mo 3d spectrum is fitted by two Gaussian doublets corresponding to molybdenum in two different oxidation states of Mo^{6+} and Mo^{5+}. As shown in Fig. 2C, the peaks located at 233.2 and 236.5 eV are assigned to the 3d doublet of Mo^{6+} and the peaks centered at 232.2 eV and 235.6 eV are ascribed to the 3d doublet of Mo^{5+}.[28] The O 1s spectrum (Fig. 2D) of the CoMoP sample is dominated by oxygen species incorporated into phosphate groups.[29] The P 2p spectrum shown in Fig. 2E discloses the presence of a single phosphorous species associated with the phosphate group.[29] The X-ray diffraction (XRD) findings represent the phase compositions of the $CoMoO_4$ and amorphous CoMoP samples. The $CoMoO_4$ sample's diffraction peaks all match up well with the monoclinic cobalt molybdenum oxide hydrate (JCPDS No. 26-0477), as shown in Fig. 2F. The reduced intensity observed in $CoMoO_4$ may be attributed to several factors, primarily the higher absorption and reduced scattering probability of the incident waves at 2θ values exceeding 30°, along with varying levels of amorphousness in the sample. Powder XRD measurements of CoMoP confirmed its amorphous structure, indicating that phosphating processes transform crystalline $CoMoO_4$ into an amorphous structure. This change enhances the catalytic performance by increasing active site accessibility and improving mass transport properties.

Electrochemical studies

Fig. 3 shows the electrochemical evaluation of the WOR on the as-prepared electrodes coupled with a three-electrode cell for linear sweep voltammetry (LSV) measurements in 1 M of KOH at a scan rate of 5 mV s^{-1}. NF/CoMoP/p-Lys shows a superior catalytic performance with an onset potential of 1.429 V *vs.* RHE for a current density (J) of *ca.* 0.1 mA cm^{-2}, which is comparable with 1.422 obtained for our recent inorganic proton relay,[14] lower than 1.45 V recently obtained for Ni–Co carbonate hydroxide (NiCoCH),[27] 1.55 for *meso*-NPC/Co_2NiO_X,[30] 1.54 for Ni_3N-coated Ni nanorods,[31] 1.53 for (Ni and Fe) S_2@MoS_2,[32] and 1.45 obtained for Co_3S_4 hybridized MoS_2–Ni_3S_2.[33] The required overpotential to reach current densities of 10 and 100 mA cm^{-2} are the significant values of 230 and 427 mV in 1.0 M KOH, respectively. The phosphating of $CoMoO_4$ causes an apparent negative shift in the overpotential at J = 50 mA cm^{-2} ($\eta_{@50\ \mathrm{mA\ cm^{-2}}}$) of the polarization curve as much as −140 mV (from 1.89 for $CoMoO_4$ to 175 V for CoMoP *vs.* RHE). Following the electropolymerization of L-lysine, $\eta_{@50\ \mathrm{mA\ cm^{-2}}}$ of the sample decreased by as much as −181 mV, indicating the role of p-lysine in promoting the PCET reaction during the WOR. The LSV obtained for NF/p-Lys well demon-

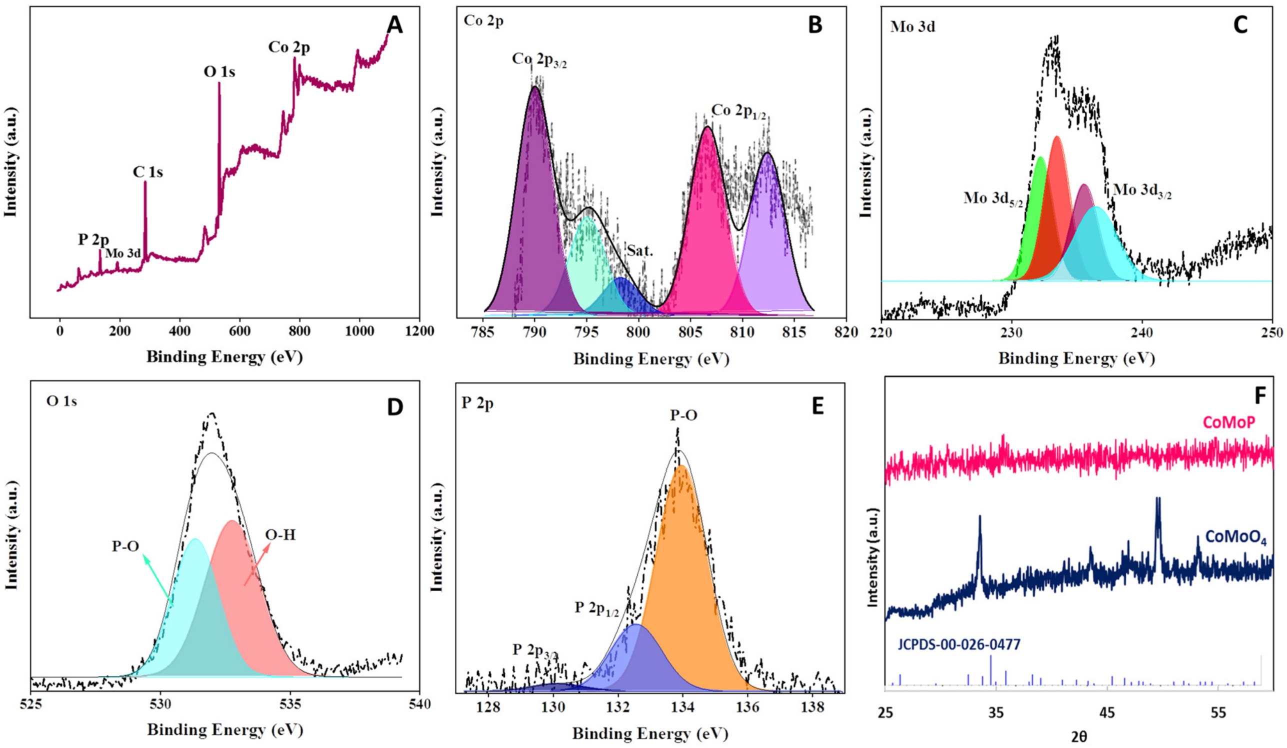

Fig. 2 XPS and XRD studies. (A) Low-resolution XPS spectra of the CoMoP powder. Deconvoluted high-resolution spectra for (B) Co 2P, (C) Mo 3d, (D) O 1s, and (E) P 2p. (F) XRD patterns of $CoMoO_4$ and the amorphous CoMoP powder.

strates the apparent role of amine residues in the performance of the OER. The current density increased by approximately 340% at a potential of 1.8 V *vs.* RHE compared to the bare NF. The equivalent increments for NF/$CoMoO_4$ and its NF/CoMoP surface were *ca.* 230% and 280%, respectively. The combination of all components in the final electrode (NF/CoMoP/p-Lys) resulted in a more than 18-fold (1800%) increase in the J value *versus* NF, indicating a significant synergetic effect upon combining the CoMoP sub-layer and p-Lys.

In Fig. 3B, the Tafel slope of NF/CoMoP/p-Lys was found to be 120 mV dec^{-1}, which is lower than the values estimated for NF (210 mV dec^{-1}), NF/$CoMoO_4$ (240 mV dec^{-1}), NF/CoMoP (140 mV dec^{-1}), NF/$CoMoO_4$/p-Lys (200 mV dec^{-1}), and NF/p-Lys (180 mV dec^{-1}). Another notable aspect in Fig. 3B is that although the WOR has been enhanced, the Tafel slopes remain greater than 120 mV dec^{-1}. Theoretically, in the low-overpotential region (<1.7 V) and based on the equation $2.303RT/(\alpha + n)F$, the Tafel slope varies from 30 to 120 mV dec^{-1}.[5,34] Conventional OER electrocatalysts with superior ET propulsion display a theoretical Tafel slope of around 40 mV dec^{-1}, indicating one step of ET before the RDS. The theoretical value of around 118 mV dec^{-1} implies an n value of zero and the first ET step as the RDS of the heterogeneous OER. One of the hypotheses behind the first ET-included RDS of the heterogeneous OER in polymeric interfaces with striking proton shuttling properties may be related to the inaccessibility of the metallic active sites (covered by the polymer) and the limitation of mass transfer, which are imperative for the first ET step ($* + OH^- \rightarrow OH* + e^-$), such that the crucial adsorption of hydroxyl ions may be the lagged step of the overall reaction. In Fig. 3C, the required overpotentials at a current density (J) 10 mA cm^{-2} (η_{10}) were calculated to be 590, 320, 400, 400, 280 and 230 mV, respectively, for NF, NF/P-Lys, NF/$CoMoO_4$, NF/CoMoP, NF/$CoMoO_4$/p-Lys, and NF/CoMoP/p-Lys. These results imply the superior catalytic activity of NF/CoMoP/P-Lys, as was used in the following electrochemical investigations. The required overpotential to reach J = 10 mA cm^{-2} for NF/CoMoP/p-Lys was compared with those of recently reported OER catalysts and the results are shown in Fig. 3D.

To investigate the role of morphology in the apparent increase of the response of NF/CoMoP/P-Lys to the NF/CoMoP sub-layer, we performed an electrochemical study to evaluate this discrepancy from the comparative kinetic OER merit. To this end, both electrodes were subjected to a scan rate study by recording CVs in 0.1 M KOH over a limited window of potentials at different sweeping rates (ν) ranging from 5 to 140 mV s^{-1} (see Fig. S6†). The plots of J *vs.* sweeping rates show two linear portions at low and high sweeping rates. The total differential capacitance (Cd, total) and its external portion (Cd, external) were measured by evaluating the slope values at low and high sweeping rates, respectively. Using the relation of $Cd_{internal} = Cd_{total} - Cd_{external}$, and employing the equation introduced for the morphology factor ($\phi = Cd_{internal}/Cd_{total}$), an

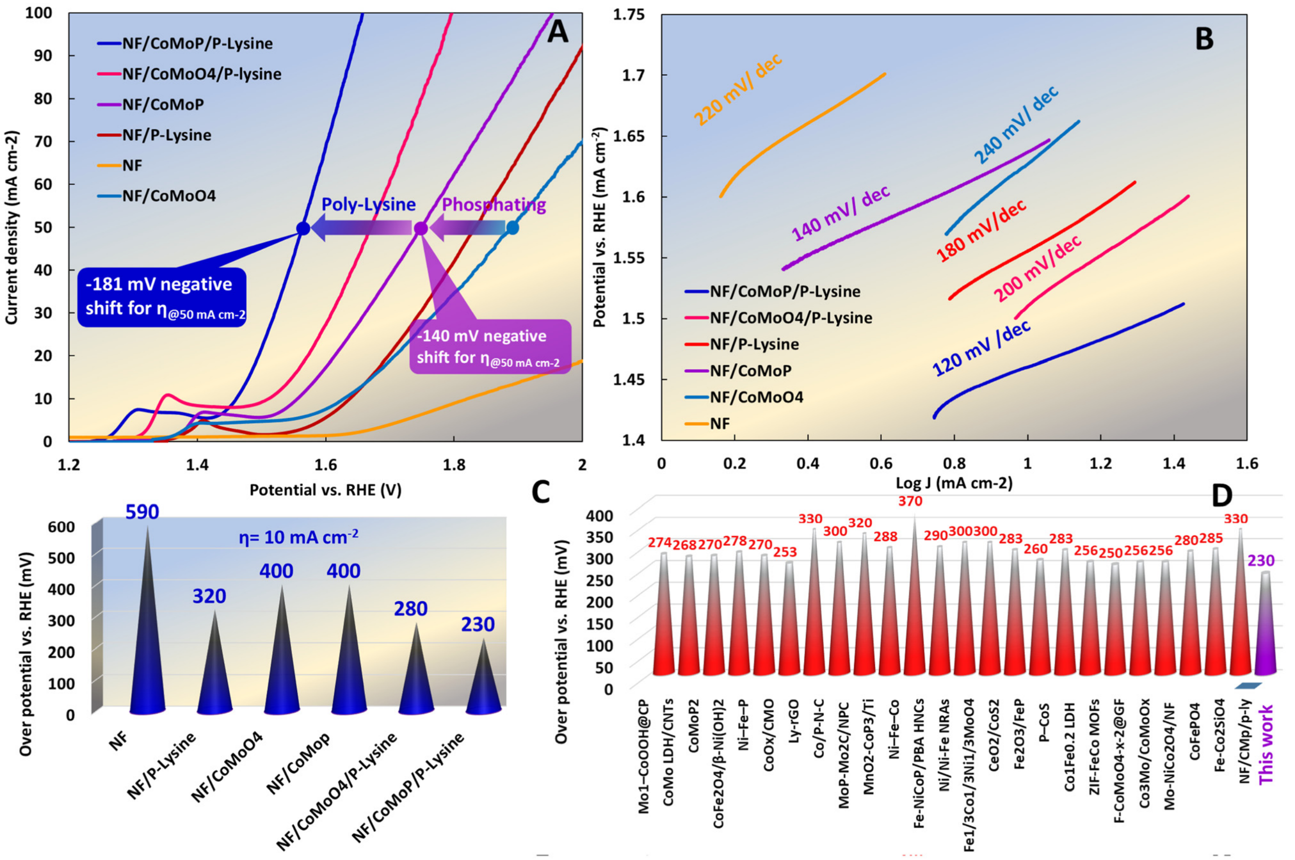

Fig. 3 Electrochemical evaluation of the OER on the as-prepared electrodes. (A) Steady-state LSV measurements at a scan rate of 5 mV s^{-1} in 1 M KOH and (B) the equivalent Tafel plot derived from the LSV, despite boosting the OER, NF/CoMoP/p-Lys shows the Tafel slope pushing to a theoretical value of 118 mV dec^{-1} in the low over potential region and seems that the first ET controls PCET as the RDS. Comparison of the required overpotentials of the (C) as-prepared electrodes together at J = 10 mA cm^{-2}. (D) Comparison of the required overpotentials of the NF/CoMoP/p-Lys electrode with the recently published OER electrocatalysts to reach J = 10 mA cm^{-2} (references are respectively from left to right).[35–58]

accumulative index was determined to elucidate the role of the morphology factor in the electrochemical response at both electrodes (see ESI note 2 for further details†). The calculated ϕ values of the NF/CoMoP/p-Lys and NF/CoMoP sub-layers were found to be 0.912 and 0.811, respectively. Values greater than 0.5 express the greater contribution of the inner surface area toward the external part in the electrochemical signal. The slight difference of ϕ values (<11%) confirms a negligible difference between the morphological factors on the electrochemical activities of both catalysts.

The efficiency of the proton relay was measured by considering the conventional Ni(II)/Ni(III) oxidation reaction, a typical heterogeneous PCET reaction, with a peak attributed to the oxidation of the $Ni(OH)_2$ passivation layer to β-NiOOH upon immersion in an alkaline solution.[59] As shown in Fig. 4, the electrodes bearing p-Lys ($NF/CoMoO_4$/p-Lys and NF/CoMoP/p-Lys) show an evident negative shift of the oxidation peak toward their relevant sub-layers ($NF/CoMoO_4$ and NF/CoMoP). The positive potential sweeping oxidizes Ni^{2+} to Ni^{3+} through a PCET process with an E_0 of *ca.* 1.41 V for $NF/CoMoO_4$, NF/CoMoP and NF/p-Lys. The most significant negative shift was observed for NF/CoMoP/p-Lys, which exhibited a predominant

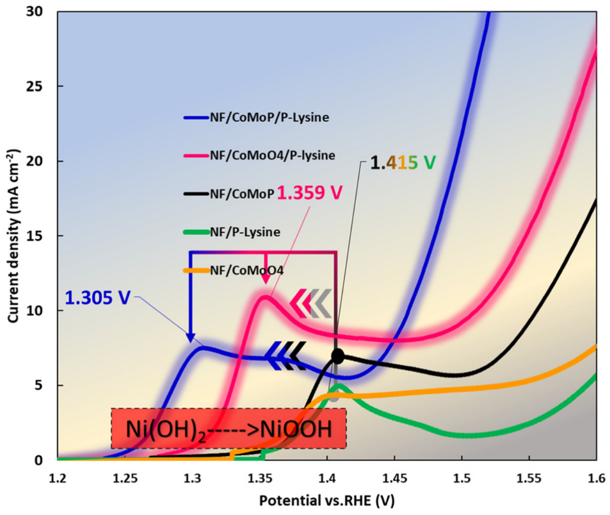

Fig. 4 The role of combination of the polymeric amine residues and interfacial phosphate groups in a typical PCET reaction. The cooperative HBN of the interfacial phosphate groups and amine residues of p-Lys in facilitating PCET proceeding the $Ni(OH)_2$/Ni–OOH redox reaction as a typical PCET reaction.

role in accelerating the PCET reaction of NF. The electropolymerization of L-lysine forms an interfacial HBN between the phosphate groups and the residual amines of the polymer. The $Ni(OH)_2$/NiOOH PCET reaction occurs at a positive potential as low as 1.305 V compared to the value of 1.359 V at NF/$CoMoO_4$/p-Lys. This occurrence is a successful early indication of the operation of proton relay even in a harsh alkaline medium (as a suitable medium for an oxidative PCET-type reaction). The above results show the effectiveness of the phosphate–snatcher interface in proton shuttling performed by the polymeric amine proton relay.

The durability of NF/CoMoP/p-Lys was tracked through a set of potentiostatic and galvanostatic pulse measurements to explain its steady-state activity and structural recoverability. Fig. 5A shows the chronopotentiometry measurements performed at different current steps of 0.02, 0.04, and 0.05 A. The chronopotentiometry measurements were performed at 1.65, 1.78 and 1.87 V *vs.* RHE (Fig. 5B). Likewise, the staircase response of chronopotentiometry measurement was considered against different current densities ranging from 30 to 200 mA cm^{-2}, as shown in Fig. 5C. The long-term durability toward the OER was examined at 1.7 V for 14 h. The accelerated PT prevents proton accumulation, spatiotemporal acidic complication and the minimum catalyst corrosion, the serious issue mostly observed in already metal-based OER electrocatalysts.[14,60,61] During the heterogeneous OER process, the surface–intermediate deprotonation is critical. The interfacial combination of polymeric amine residues and proximal phosphate groups can accelerate the deprotonation steps from –OH to –O* and –OOH to –OO* during the OER and directly influence PCET's efficiency during the OER,[5,52,62] as shown in Fig. 3, as a typical PCET reaction even in alkaline pH values, which is a preferred medium for the oxidative PCET reaction. In order to explore the possible changes in electrode identity, EDXA was carried out before and after electrolysis. No significant changes were observed in the oxygen content. This is in contrast to our previously studied precatalyst[22] with a polymer-free interface, where the interfacial metallic active site underwent slight surface transformation to an oxy-hydroxide protective layer with an apparent increase in the oxygen content (as a qualitative confirmation). This transformation was intended to preserve underlayers from further oxidation. The EDXA

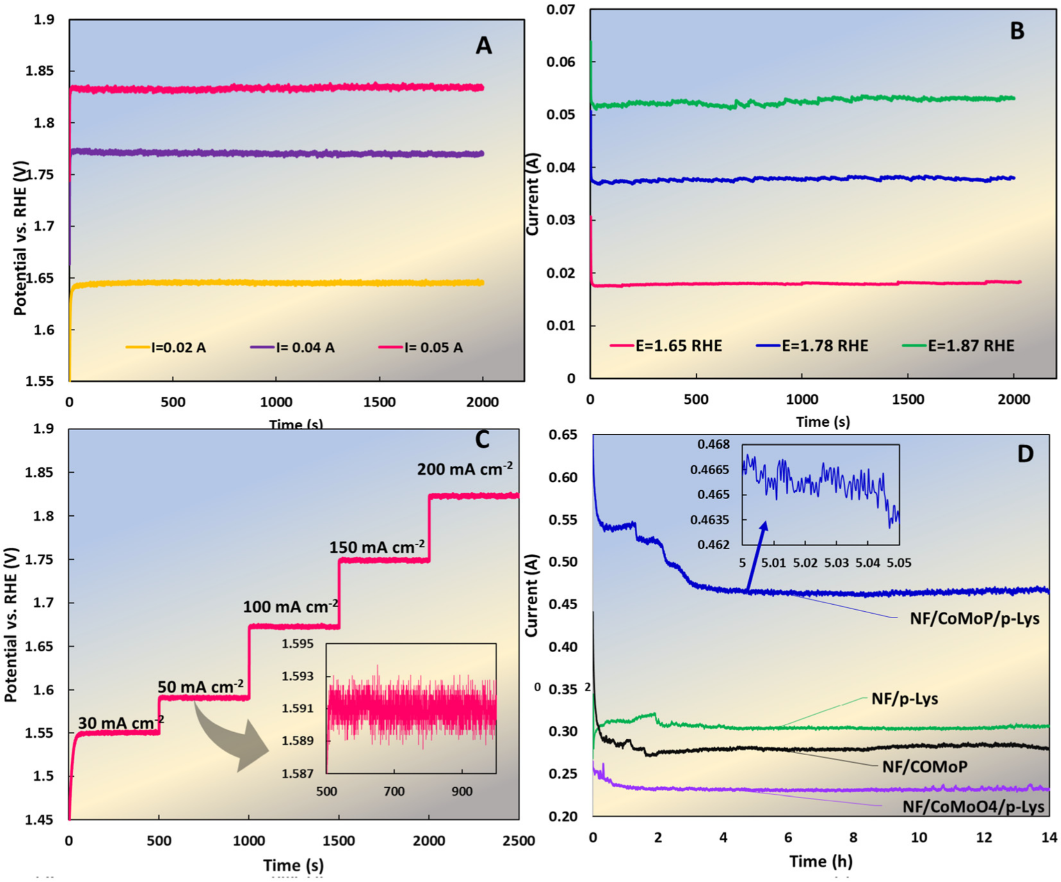

Fig. 5 Chrono-response measurements. (A) Chronopotentiometric curve obtained with the NF/CoMoP/p-Lys electrode in 1 M KOH at three constant currents of 0.02, 0.04, and 0.05 A without iR compensation. (B) Chronoamperometric curves obtained with the NF/CoMoP/p-Lys electrode in 1 M KOH at three constant potentials of 1.65, 1.78, and 1.87 *vs.* RHE. (C) Staircase response of the chronopotentiometry measurement against different current steps ranging from 30 to 200 mA cm^{-2}. (D) Long-term chronoamperometric measurement performed at 1.7 V *vs.* RHE for 14 h with appropriate response stability after initial equilibration.

mapping results shown Fig. S7 and S8† indicate a minor change in oxygen contents that is a prior indication of possible surface oxidation in positive potentials in an alkaline medium. This can be related to the protective identity of the polymeric layer and also efficient proton shuttling by the polymer to prevent corrosion caused by spatiotemporal generation of protons. A comparative attenuated total reflection analysis was performed before and after electrolysis to explore possible change of the polymer structure (Fig. S9†). The results illustrate no evident alterations of the main stretching modes of the amide bands (I and II) at around 1605 $\mathrm{cm^{-1}}$ and also the NH stretching bond at around 3375 $\mathrm{cm^{-1}}$.

Kinetic isotope effect studies

Protoeo/deutero isotopic studies give deep insight into the competition between PT and ET as parts of PCET as well as the kind of rate-determining step, ET or PT participated in the heterogeneous OER.[5,6,14] The key function is the kinetic isotopic effect (KIE) calculated using:

$$\mathrm{KIE} = \frac{j_{\mathrm{H_2O}}(K_{\mathrm{H_2O}})}{j_{\mathrm{D_2O}}(K_{\mathrm{D_2}O})}.$$

Here, the heterogeneous rate constants ($K_{\mathrm{H^2O}}$ and $K_{\mathrm{D^2O}}$) are directly proportional to the *J* values, an acceptable assumption for the surface-controlled reactions (see ESI note†). The KIE values >1.5 conveys a primary isotope effect (PKIE) with a PT involved in the RDS or at least in one of the steps affecting the kinetic of PCET. The KIE < 1.5 suggests a secondary kinetic isotope effect (SKIE), indicating that the rate-determining step (RDS) of proton-coupled electron transfer (PCET) does not involve the breaking of an O–H bond.[63,64] Electrochemical measurements were independently carried out in H_2O and D_2O at various pH (D) values (pD = $\mathrm{pH_{read}}$ + 0.41).[65] The pH (D) of the water and deuterium solutions were adjusted respectively using KOH and K_3PO_4 to 13 and 12.6. Since there was no evidence of OER activity dependence on K_3PO_4 in the atom proton transfer studies,[5] K_3PO_4 was used for the adjustment of pD (figure not shown). Fig. 5A–F show the LSVs obtained for the NF, NF/$CoMoO_4$, NF/CoMoP, NF/p-Lys, NF/$CoMoO_4$/p-Lys and NF/CoMoP/p-Lys electrodes in D_2O (blue curves, b) and H_2O (red curves, a), respectively. The LSVs recorded in deutero solutions showed lower current densities compared to those recorded in proteo solution at all overpotentials. As shown in Fig. 5A and B, upon substitution of H with D, NF and NF/$CoMoO_4$ show a significant decrease in the *J* value, indicating the contribution of PT in the RDS of the OER.[66] In contrast, the separation of the *J* values in NF/CoMoP diminished when H is substituted with D (KIE ≥ 1.5) and implicitly discloses the capability of interfacial phosphate groups on PT even in an alkaline medium as a well-known conventional medium for oxidative PCET reactions (Fig. 6C). The insets represent the potential dependency of KIEs with average values of 2.7, 1.71 and 1.60 respectively at NF, NF/$CoMoO_4$ and NF/CoMoP over the potential range of 1.6–1.9 V *vs.* RHE, indicating a PKIE and O–H bond cleavage in the RDS.[6,14] The current differences significantly diminished for NF/p-Lys, NF/$CoMoO_4$/p-Lys and NF/CoMoP/p-Lys (Fig. 5D–F) so that the *J* values in D_2O get the closest distance to those in H_2O. At 1.7 *vs.* RHE, the KIEs get average values of 1.24, 1.17 and 1.11, respectively. These values provide secondary KIEs (SKIEs), in which no O–H bond cleavage is observed in the RDS of the OER. The lowest KIE value observed was 1.09 (at 1.9 V *vs.* RHE) for NF/CoMoP/p-Lys, indicating that the synergy between pendant amine groups and interfacial phosphate groups in the sub-layer effectively promotes proton transfer during the oxygen evolution reaction in an alkaline environment. It is worth noting that the magnitudes of most SKIEs are thought to decrease as the transition state structure changes from product-like to reactant-like transition, in contrast to the PKIE that shows a symmetrical transition state and small KIEs for either of early or a lagged transition state.[5,6] The absolute SKIEs observed in Fig. 5D–F originated from changes in the force field upon transferring reactants to the transition state of the reaction RDS. The magnitude of the SKIE is controlled by the zero-point energy directly tied to the tight overlapping of vibrational wave functions and the efficiency of H-bonding and the proximity of the proton donor–acceptor in the interfacial surface-confined p-Lys#phosphate hydrogen bonded network. Providing this condition makes possible the Grotthuss mechanism (proton hopping) and practically blocks the natural diffusion of protonic reaction species (H^+, OH^- and H_2O) to/from the current collector, as was identified by observing the extreme case of the finite length Warburg (FLW) impedance (Gerischer impedance) in the following impedance section.

The redox behavior of the $Ni(OH)_2$/NiOOH oxidation peak was investigated in both proteo and duetero solutions. The substitution of H with D causes a significant change in the diving force, resulting in a positive shift in the peak potential of Ni$(OD)_2$/NiOOD compared to the $Ni(OH)_2$/NiOOH pair.[67] The observed change can be attributed to the shorter O–D bond length compared to that of O–H, which introduces an unfavorable energetic factor in PCET.[68] The linear sweep voltammograms (LSVs) of NF/CoMoP/p-Lys shown in Fig. 6H reveal identical peak potentials, suggesting that the kinetic barriers are comparable in both hydrogen and deuterium solutions.

Proton inventory (PI) studies

Following analysis of the KIE, the number of active protonic sites involved in the catalytic process was determined *via* the proton inventory, a particular kind of solvent isotope effect.[69–71] Herein, the relationship between partial deputation of water molecules and OER activity serves the level of concreteness in PCET.[71,72] Plotting the recorded change in the rate constant ($k \approx j$) in the presence of D_2O *versus* the mole fraction of deuterium oxide in the mixed solutions provides useful information. Fig. 6(A–D) show the LSVs and equivalent plots of J_n/J_H (k_n/k_H) on the mole fraction of D_2O in a mixture of the D_2O/H_2O at NF/$CMoO_4$, NF/CoMoP, NF/$CoMoO_4$/p-Lys and NF/CoMoP/p-Lys electrodes, respectively. As shown in Fig. 7A and B, a linear graph the plot of Jn/J0 *vs.* mole fraction of D_2O suggests a single site and a concerted mechanism of PCET, but a non-linear tendency indicates the contribution of mul-

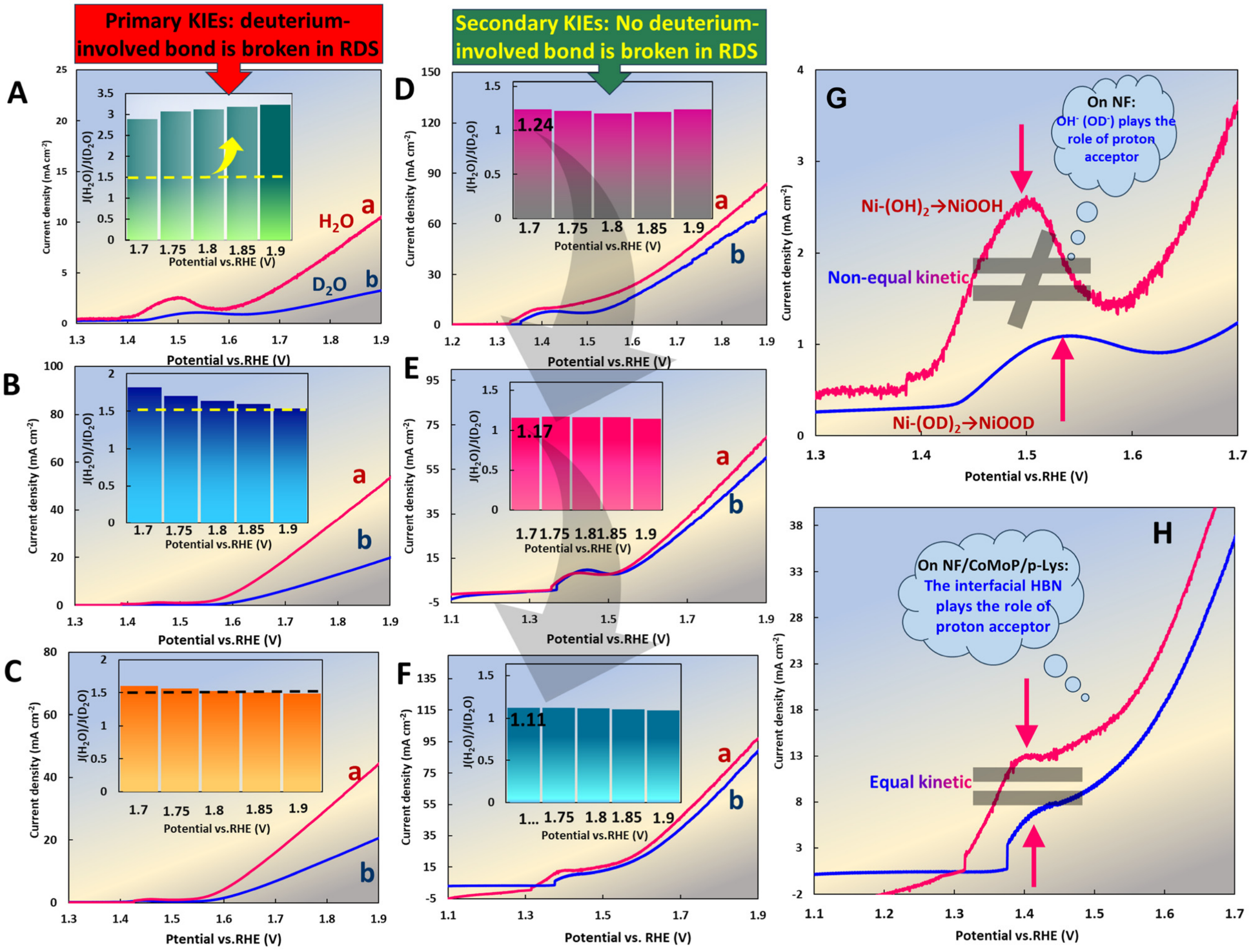

Fig. 6 Kinetic isotopic effect studies. LSVs recorded in H_2O (red) and D_2O (blue) for the (A) NF, (B)NF/$CoMoO_4$, (C) NF/CoMoP, (D) NF/p-Lys, (E) NF/$CoMoO_4$/p-Lys and (F) NF/CoMoP/p-Lys electrodes. Comparison of the oxidation peak positions in proteo (red) and duetero (blue) solutions for Ni^{2+}/Ni^{3+} taken for (G) NF and (H) NF/CoMoP/p-Lys, demonstrating the undeniable role of the proton relay groups in the kinetic acceleration of the $Ni(OH)_2$/Ni-OOH redox couple as a typical PCET reaction.

tiple sites, as it is defined by the terms of charge relay or the proton shuttle process.[72] As is shown in Fig. 7(A and B), a plot of J_n/J_0 *vs.* nD_2O obtained for the NF/$CoMoO_4$ and NF/CoMoP electrodes displays a linear behavior, This is an indicator for the transition state stabilized with a single protonic interaction.[71] The plot sketched for the NF/$CoMoO_4$/p-Lys and NF/CoMoP/p-Lys electrodes (Fig. 7C and D) shows a deviation from linearity, a criterion of non-concreteness during PCET.[70,71] The incorporation of interfacial phosphate groups significantly intensifies the non-linearity of the plot.[71] The plots were plotted using a modified Kresge–Gross–Butler equation as follows:[5]

$$J_n = J_0[1 - n + n\varphi]Z^n$$

where J_n and J_0 are the current densities in the protic solvent and different mole fractions of the deuterated solvent in water, respectively. The symbol φ denotes the isotopic fractionation factor, which evaluates the deuterium preference of the hydrogenic sites in a reactant or transition state toward the deuterium preference of the water molecules.[71] The magnitude of φ depends directly on the adjacency functions of the isotopic sites, a criterion of the HB strength.[5,62] The typical values of φ for weak hydrogen bonds are 1.0–1.2, while very strong hydrogen bonds show values less than 0.5.[71] Z denotes the Z-effect, which measures a combination of individual weak isotope effects originating from multiple equivalent hydrogenic sites.[5,62] Fig. 7A–C show a linear dependency (Fig. 7C displays a slight deviation of linearity) that coincided with the $J_n/J_0 = 1 - n + 0.33n$ equation, indicating a transition state stabilized with a single protonic interaction.[71] For NF/CoMoP/p-Lys (Fig. 7D), a non-linear dome-shaped behavior with a fitting parameter of $Z = 1.594$ was observed. The large Z-effect ($Z > 1$) shows an aggregate inverse isotope effect at the active site of the HBN. The φ values 0.534 ($\phi < 1$) at 1.6 V (and the values of 0.514, 0.491 and 0.469 at 1.65, 1.7 and 1.75 V, respectively) demonstrate a strong HB.[5,62,71] Herein, we did not consider the participation of the isotope effect originating from the reaction intermediate and other polymer functional groups with relatively weaker H-bond interactions, a small KIE, and φ values close to

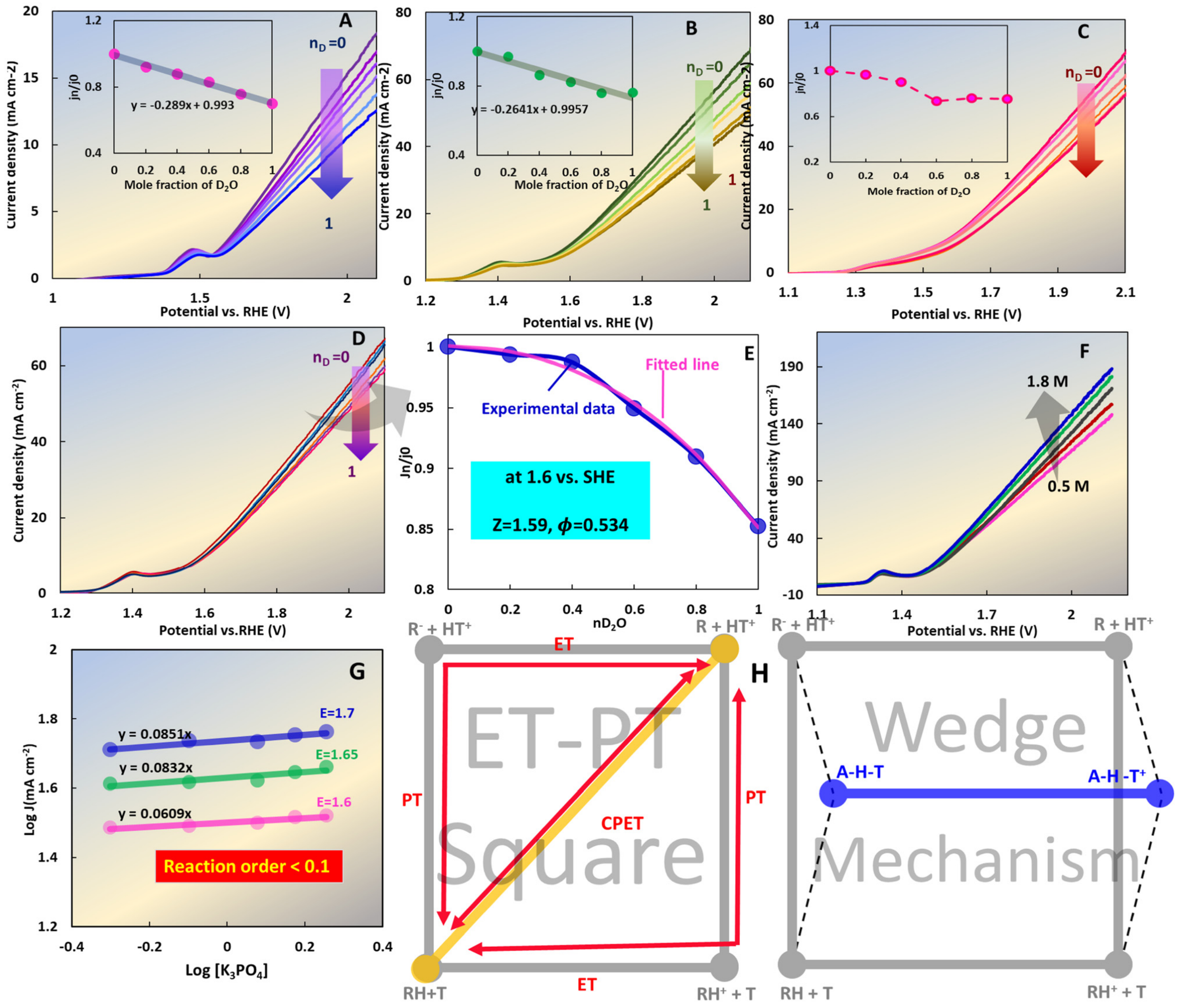

Fig. 7 Results of proton inventory studies. LSVs obtained in a mixed solution of D_2O and H_2O with different mole fractions of D_2O for (A) NF/$CoMoO_4$, (B) NF/CoMoP, (C) NF/$CoMoO_4$/p-Lys and (D) NF/CoMoP/p-Lys. The insets in (A–C) show the corresponding plots of J_n/J_0 (J_0 in H_2O and J_n in different mole fractions of D_2O) *vs.* the mole fraction of D_2O. (E) Corresponding experimental and fitted lines for the plots of J_n/J_0 *vs.* n_D for NF/CoMoP/p-Lys (the inset depicts the φ and *Z*-factors obtained from the fitting parameters of the Kresge–Gross–Butler equation). (F) LSVs recorded for NF/CoMoP/p-Lys in 0.1 M KOH and at different concentrations of K_3PO_4 (0.5 to 1.8 M). (G) Plot of log *J* against log [K_3PO_4] indicating the negligible reaction orders (lower than 0.1) for the OER with a Lewis base, K_3PO_4, at different potentials. (H) PCET schemes (wedge *vs.* conventional ETPT) for a typical half-reaction $RH + T \xrightarrow{-e} R + HT^+$, where T denotes the proton acceptor residues of the HBN and RH is the surface adsorbed protonic species (OH* or OOH*).

one, which does not significantly contribute to the overall isotope effect.

The results of the KIE, PI, Tafel slopes and Gerischer impedance studies are employed to suggest an overall mechanism for PT and H-bond equilibria for illustrating the transition state of OERs enhanced by the as-fabricated proton relay on an interfacial HBN that acts as an intermediate in the proton transfer (PT). This process resembles a wedge mechanism (see Fig. 7H) and requires increased stability from H-bonding in the transition state of PET, considering CPET serves a significant KIE > 1.5 due to PT occurring alongside ET in the rate-determining step.[5] To differentiate between the CPET and the wedge mechanisms in CPET, assessing the kinetic isotope effect (KIE) is essential. In an n-CPET pathway (as approved by pH and PI studies), the wedge mechanism gets two primary features: (1) a low SKIE and (2) an ET-involved RDS, both of which were observed in this study. Further evidence for the existence of this pathway includes the low barrier characteristic of the H-bond, as indicated by the proton inventory data, where a small fractionation factor reflects a low-barrier transition-state HB. In addition, the Gerischer impedance suggests a strong affinity for H-bonding to the phosphate-p-Lys HBN. A wedge mechanism shows either a large or a small KIE, depending on the type of concerted or non-concerted mechanism, respectively, therefore it can complete the puzzles of the PET mechanism in conjunction with the KIE, Gerischer analyses, and RHE scale pH investigations.[5]

The application of a Lewis base (multivalent anions) that serves as a proton acceptor can enhance the catalytic reactions' kinetics if the RDS of the WOR is directly tied to the PT, the process that is known as "atom proton transfer" (APT) study.[73] Here, we measured the OER activity against different concentrations of K_3PO_4 (from 0.5 to 1.8 M). The corresponding LSVs shown in Fig. 7E present negligible changes in the current density. Fig. 7F shows the related plot of $\log J$ as a function of $\log[K_3PO_4]$ at different potentials of 1.6, 1.65 and 1.7 V. The order of all reactions against phosphate were lower than 0.1 (*i.e.*, 0.063, 0.085 and 0.083 at different over potentials), which indicate that no PT involves in the RDS of the OER on the NF/CoMoP/p-Lys electrode. Indeed, the contribution of a Lewis base such as K_3PO_4 offers an alternative CPET path to approach the driving force of the pH-dependent equilibrium, a competition strategy that aborted here.

PH studies on the RHE scale

The pH studies on the RHE scale were performed to obtain a comprehensive insight into the type of the PCET mechanism in concerted (CPET) or non-concerted (stepwise, *n*-CPET) mechanisms driven by the as-prepared electrodes. To compensate the change in thermodynamic driving force at different pH values, the catalytic activity was tracked on the RHE scale. The multi-step PCET reactions conventionally proceed through two pathways: CPET or n-CPET. CPET denotes a pH-dependent process that involves the concurrent transfer of protons and electrons almost observed in metallic-based OER electrocatalysts.[5] The pH-dependent OER activity on the RHE scale characterizes an n-CPET process. Traditionally, the probability of a stepwise approach is intensified by stabilizing proton species intermediates through H-bond complexes created during interfacial PCET reactions. The proposed mechanism for characterizing the transition state of OERs enhanced by the phosphate-p-Lys hydrogen-bonded network (HBN) is centered around an H-bond complex that forms as an intermediate during the proton transfer (PT). This mechanism resembles the wedge mechanism, describing the increased stability *via* H-bonding at the transition state of PET.[5,74,75] In an n-CPET pathway, the wedge mechanism has two key features that existed in this work: (1) a low KIE and (2) the ET-involved RDS. The electrochemical measurements were carried out on the NF, NF/p-Lys, NF/$CoMoO_4$, NF/$CoMoO_4$/p-Lys, NF/CoMoP and NF/CoMoP/p-Lys electrodes over the pH range of 10–13 and the results are shown in Fig. 8A. The pH-independent activity

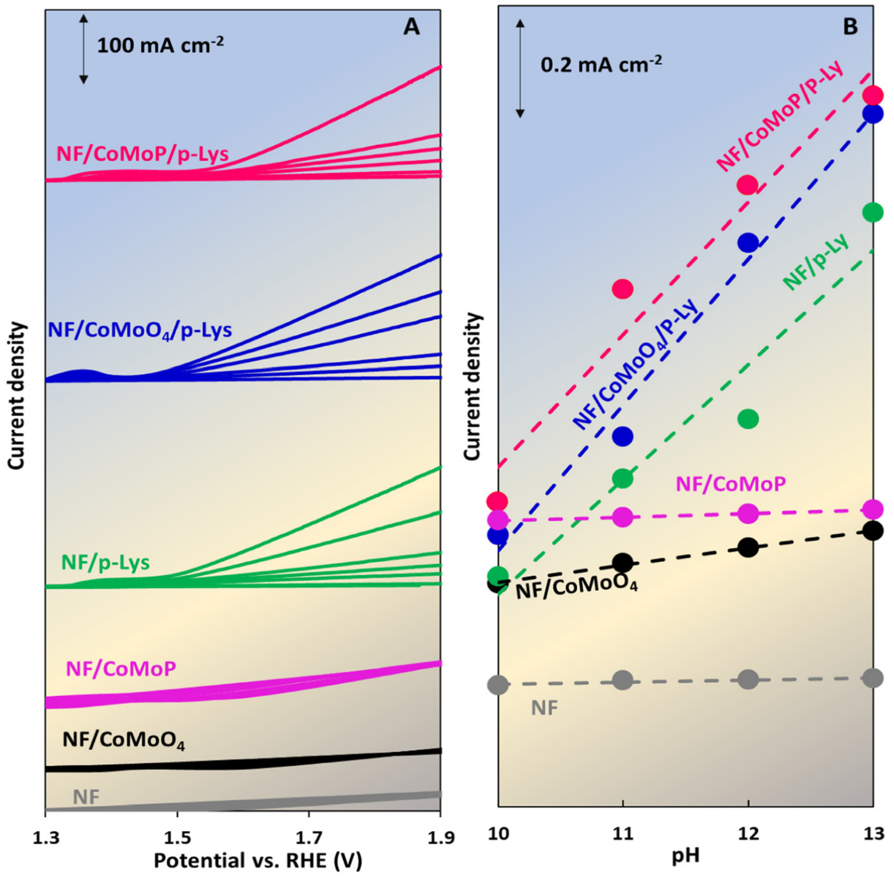

Fig. 8 PH-dependent OER activity on the RHE scale. (A) LSVs obtained over the pH range of 10–13. (B) Specific OER activity at 1.65 V *versus* RHE as a function of pH (fractional reaction orders of 0.0–0.2 at different potentials).

(zero-order reaction) of the obtained LSVs on NF, NF/$CoMoO_4$, and NF/CoMoP indicates an expectable CPET mechanism. Meanwhile, the OER activities of NF/p-Lys, NF/$CoMoO_4$/p-Lys and NF/CoMoP/p-Lys were found to increase with increasing pH. The pH-dependent OER activity imparts a non-concerted mechanism.[76] For NF, NF/$CoMoO_4$, NF/CoMoP, NF/$CoMoO_4$/p-Lys and NF/CoMoP/p-Lys, the reaction orders, calculated form the slope of the plot of log *J* *vs.* pH (inset of Fig. 8B) at a constant potential 1.65 V, show values ranged from around 0.0–0.20, respectively. Moreover, as shown in Fig. 8B, these obtained slopes of the NF/$CoMoO_4$/p-Lys and NF/p-Lys electrodes and especially that of the NF/CoMoP/p-Lys electrode because of having the comprehensive H-bond bridging in order to indirect proton transfer in the catalysts nerve are much higher than those of the NF, NF/$CoMoO_4$ and NF/CoMoP electrodes. Such a fractional non-zero reaction order approves an n-CPET process in which protons involve in some complex chains and side reactions.[5]

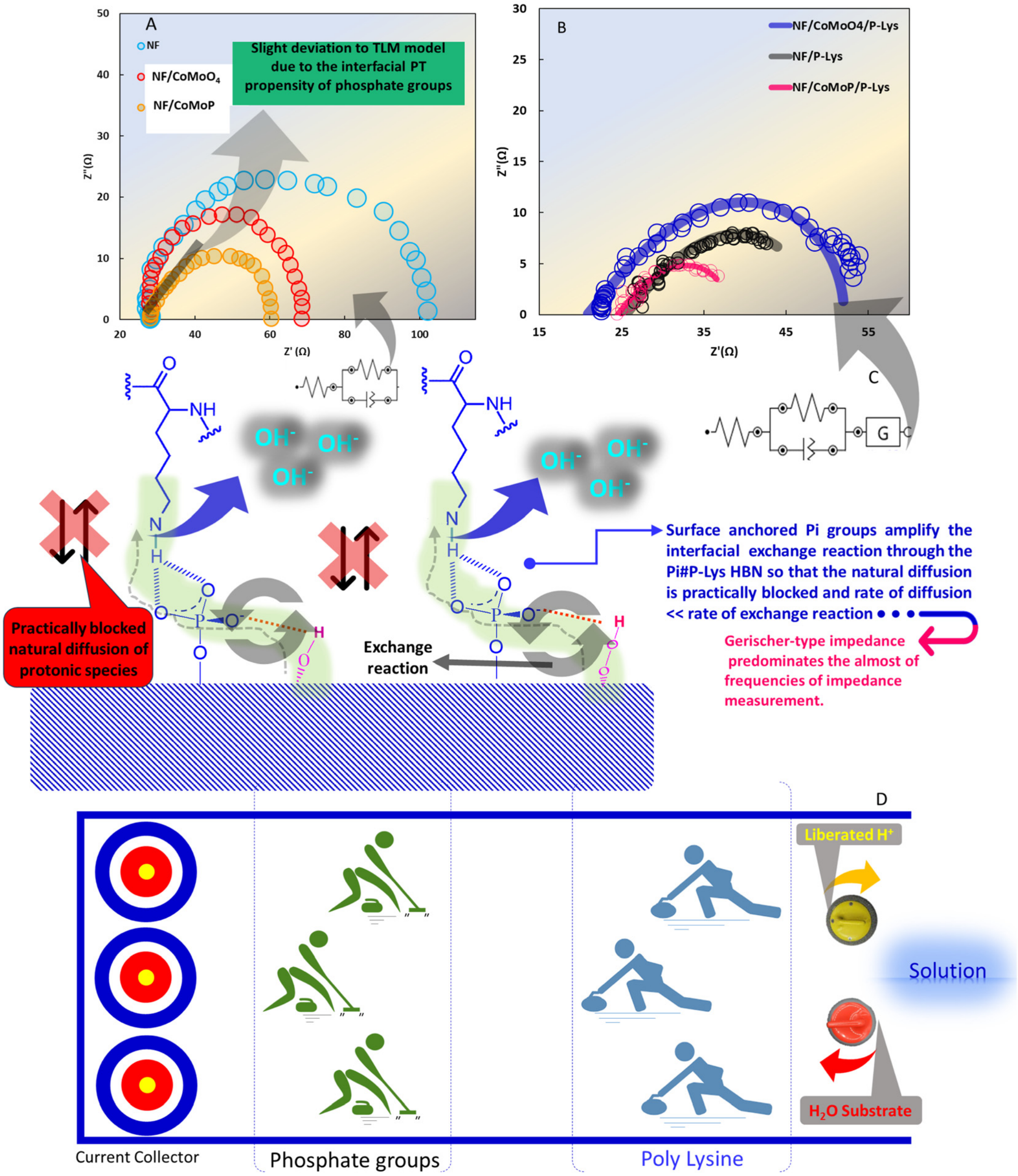

Fig. 9 Impedance studies and the proposed mechanistic approach for proton shuttling. The Nyquist plots of the (A) NF, NF/$CoMoO_4$ and NF/CoMoP electrodes in 1 M KOH. (B) Gerischer impedance and CEC mechanisms for different substrates bearing proton relays. The Nyquist plots were recorded in 1 M KOH for the NF/$CoMoO_4$/p-Lys, NF/p-Lys and NF/CoMoP/p-Lys electrodes. (C) The combinational role of the surface-bonded phosphate groups and interfacial amine residues in proton hopping and blocking natural diffusion. (D) The reciprocal curling-resembling proton shuttling role of the amine and phosphate sub-layers through a TLM model (CEC) mechanism approved by G impedance.

Electrochemical impedance spectroscopy

Fig. 9 shows the Nyquist plot obtained in 1 M KOH for the NF, NF/$CoMoO_4$, NF/CoMoP (Fig. 9A) NF/p-Lys, NF/$CoMoO_4$/p-Lys, and NF/CoMoP/p-Lys (Fig. 9B) electrodes. As shown in Fig. 9A, the conventional behavior with a symmetrical arc due to ET in the low/high-frequency region is shown in the Nyquist plots of NF, NF/$CoMoO_4$, and NF/CoMoP, which indicates a diffusion-controlled process. In contrast, the same substrates that carried pendant amine/phosphate–interface proton relies displayed a semicircle in the low-frequency region and instead of rotating on the horizontal axis, it keeps going through a 45° transmission line to high frequencies (Fig. 9B). The electrochemical reactions that precede and follow the simultaneous diffusion and chemical reactions in the diffusion layer are represented by this feature of the semi-infinitive behavior (transmission line model, TLM). The resulting data prove the preparation of new proton transfer ways through an H-bonding network between the pendant amine groups on the phosphate surface that disturb natural diffusing ways.

The competition between the rates of the diffusion and chemical reaction processes would result in different types of TLM being observed. A chemical–electrochemical–chemical type mechanism (CEC) is indicated by the observation of the TLM in the Nyquist plot from a physical perspective.[5,64] In summary, two distinct but similar types of TLM models will be used to analyze the obtained impedance data in order to illustrate various interfacial physical phenomena. Next, in order to fit the TLM data, we looked at two models made up of Gerischer (G) and finite-length Warburg (FLW). The pure Gerischer model exhibits a transmission line with a 45° slope in the high-frequency region.

Strikingly, the Nyquist plot displays a limited Warburg portion in the high frequency region and an arc in the low frequency region. In this case, the dc resistance is expressed as:

$$R_{\mathrm{dc}} = \frac{1}{3}R_{\mathrm{diff}} + R_{\mathrm{exch}} \tag{1}$$

where $R_{\mathrm{exch}} < R_{\mathrm{diff}}$ (the TLM in the high frequency region). This can be simplified from the cotangent relationship created for the TLM general cases, as shown in the following equation: If the time scale of the exchange reaction is shorter than the natural diffusion across the interfacial layer ($\omega_{\mathrm{exch}} \gg \omega_{\mathrm{diff}}$), the diffusing proton species (H^+ and H_2O) are snatched before being placed in the path of natural diffusion. The model corresponding to this condition is called Gerischer's impedance, and the dc resistance has the simplified form of:

$$Z_{\omega} = \sqrt{\frac{R_{\mathrm{diff}} \times R_{\mathrm{exch}}}{1 + \frac{j_{\omega}}{\omega_{\mathrm{exch}}}}} \tag{2}$$

$$\sqrt{R_{\mathrm{exch}}R_{\mathrm{diff}}}. \tag{3}$$

At the interface between the polymer and the electrolyte, the transport resistance and the exchange (adsorption) resistance are denoted by letters R_{s} and R_{ex}. The angular frequency is represented by ω and the rate of a chemical reaction is represented by $1/k$. RG is the product of R_{diff} and R_{exch}, even though they cannot be calculated independently.[68] When the G element manifests at high frequencies, it practically blocks natural diffusion at the polymer residue, allowing the released protons to effectively move through the inner wall of the phosphate surface that has been functionalized with a pendant amine. As can be seen in Fig. 9B, the red curve substrates show an apparent shrinking that confirms the reducing time scale of the exchange reaction as the origin of the proton hopping pathway toward natural diffusion. Actually, the pendant amine network derived from the poly lysine in the NF/$CoMoO_4$/p-Lys and NF/p-Lys catalysts (no phosphate substrate) act as the effective proton acceptor adjacent to the O*H and OO*H intermediates and the stabilized intermediates lead to an accelerated proton transfer (Fig. 9c). Fig. 9D shows the performance of the proposed bifunctional proton hopping system through reinforced sliding of stones (protonic species) as the role of amine snatchers and brushing of the path as the complementary sweeper role of phosphate groups, leading to a straighter path propelled by protons with less curl.

Conclusions

A bifunctional layered Lewis base HBN contributes to the shuttling of protonic species during the OER through a fast pre- and post-exchange reaction during the OER. The exchange reaction rate exceeded the natural transport within the diffusion layer, as experimentally supported by the extended case of TLM, called Gerischer impedance. Thanks to the exchange reaction on the Lewis base amine sites, PCET proceeds through downhill PT as studied *via* the KIE and proton inventory studies. The SKIE (KIE ≈ 1.1) indicates no PT participation in the RDS of PCET, where a Tafel slope around the theoretical value of 118 mV dec^{-1} supposes the first ET step of the OER as the RDS. The LSV studies conclude the cooperation of the poly-Lys and phosphate sub-layers. The non-linear dependency of proton inventory studies indicates the contribution of multiple sites, a proton shuttling process. The G impedance in the high-frequency region of EIS corroborates a blocked natural transfer and a CEC mechanism of the OER on the suggested PCET catalyst. The urchin-like morphology with high functionality and high-ordered sub-nanometric corridors can provide abundant diffusion pathways for ion transport and gain low resistance for electrolyte ion movement.

Data availability

The datasets used and/or analysed during the current study are available from the corresponding author on reasonable request.

Conflicts of interest

There are no conflicts to declare.

Acknowledgement

There was not any funding to declare for this work.

References

1 Authors greatly thank to Mr Kumayl Sadr-Javadi foH. Li, H. Shang, Y. Shi, R. Yakimova, M. Syväjärvi, L. Zhang and J. Sun, *J. Mater. Chem. A*, 2018, **6**, 24358–24366.

2 J. M. Savéant, *Angew. Chem., Int. Ed.*, 2019, **58**, 2125–2128.

3 M. Shamsipur and A. Pashabadi, *Coord. Chem. Rev.*, 2018, **374**, 153–172.

4 C. Liang, X. Liu, C. Ling, F. Guo, M. Li, X. Zhang, Y. Shu, H. Sun, Z. Ai and L. Zhang, *Appl. Catal., B*, 2024, **352**, 124025.

5 M. Shamsipur, M. Ardeshiri, A. A. Taherpour and A. Pashabadi, *J. Mater. Chem. A*, 2021, **9**, 2937–2947.

6 R. Azizi, M. Shamsipur, A. A. Taherpour and A. Pashabadi, *J. Mater. Chem. A*, 2023, **11**, 1491–1502.

7 M. Shamsipur, A. Ghavidast and A. Pashabadi, *Acta Pharm. Sin. B*, 2023, **13**, 2844–2876.

8 M. Shamsipur and A. Pashabadi, *Coord. Chem. Rev.*, 2019, **401**, 213068.

9 M. Shamsipur and A. Pashabadi, *ChemElectroChem*, 2023, **10**, e202300423.

10 Y. Umena, K. Kawakami, J.-R. Shen and N. Kamiya, *Nature*, 2011, **473**, 55–60.

11 H. Dau, I. Zaharieva and M. Haumann, *Curr. Opin. Chem. Biol.*, 2012, **16**, 3–10.

12 H. Dau and M. Haumann, *Coord. Chem. Rev.*, 2008, **252**, 273–295.

13 N. Sakashita, H. Ishikita and K. Saito, *Phys. Chem. Chem. Phys.*, 2020, **22**, 15831–15841.

14 K. Ahanjan, M. Shamsipur, N. Hassani, M. Neek-Amal and A. Pashabadi, *J. Phys. Chem. C*, 2023, **127**, 24508–24522.

15 Y. Surendranath, M. Dinca and D. G. Nocera, *J. Am. Chem. Soc.*, 2009, **131**, 2615–2620.

16 F. Zeng, J. Li, J. P. Hofmann, T. Bisswanger, C. Stampfer, H. Hartmann, A. Besmehn, S. Palkovits and R. Palkovits, *Catal. Sci. Technol.*, 2021, **11**, 1039–1048.

17 H. Zhao and Z. Y. Yuan, *ChemCatChem*, 2020, **12**, 3797–3810.

18 X. Mu, J. Du, Y. Zhang, Z. Liang, H. Wang, B. Huang, J. Zhou, X. Pan, Z. Zhang and E. Xie, *ACS Appl. Mater. Interfaces*, 2017, **9**, 35775–35784.

19 S. Li, N. Yang, L. Liao, Y. Luo, S. Wang, F. Cao, W. Zhou, D. Huang and H. Chen, *ACS Appl. Mater. Interfaces*, 2018, **10**, 37038–37045.

20 Y. Feng, L. Liu, J. Liang, W. Yao, B. Tian, C. Jiang and W. Wu, *J. Power Sources*, 2019, **433**, 126676.

21 Y. Shen, Z. Li, Z. Cui, K. Zhang, R. Zou, F. Yang and K. Xu, *J. Mater. Chem. A*, 2020, **8**, 21044–21052.

22 K. Ahanjan, M. Shamsipur, A. A. Taherpour and A. Pashabadi, *Electrochim. Acta*, 2022, **433**, 141249.

23 L. Yu, L. Wu, B. McElhenny, S. Song, D. Luo, F. Zhang, Y. Yu, S. Chen and Z. Ren, *Energy Environ. Sci.*, 2020, **13**, 3439–3446.

24 A. T. Carvalho, K. Szeler, K. Vavitsas, J. Åqvist and S. C. Kamerlin, *Arch. Biochem. Biophys.*, 2015, **582**, 80–90.

25 C. A. Manrique-Bastidas, P. Sundaram, P. J. Resto, N. Mina-Camilde and S. P. Hernandez-Rivera, *Journal of Molecular and Engineering Materials*, 2018, **6**, 1850007.

26 L. Marsich, A. Bonifacio, S. Mandal, S. Krol, C. Beleites and V. Sergo, *Langmuir*, 2012, **28**, 13166–13171.

27 K. Karthick, S. Subhashini, R. Kumar, S. Sethuram Markandaraj, M. M. Teepikha and S. Kundu, *Inorg. Chem.*, 2020, **59**, 16690–16702.

28 F. Xie, W. C. Choy, C. Wang, X. Li, S. Zhang and J. Hou, *Adv. Mater.*, 2013, **25**, 2051–2055.

29 R. Zhang, G. van Straaten, V. Di Palma, G. Zafeiropoulos, M. C. van de Sanden, W. M. Kessels, M. N. Tsampas and M. Creatore, *ACS Catal.*, 2021, **11**, 2774–2785.

30 J. Wang and H. C. Zeng, *ACS Appl. Mater. Interfaces*, 2020, **12**, 50324–50332.

31 H. Wang, J. Xiong, X. Cheng, M. Fritz, A. Ispas, A. Bund, G. Chen, D. Wang and P. Schaaf, *ACS Appl. Nano Mater.*, 2020, **3**, 10986–10995.

32 Y. Liu, S. Jiang, S. Li, L. Zhou, Z. Li, J. Li and M. Shao, *Appl. Catal., B*, 2019, **247**, 107–114.

33 A. Muthurasu, G. P. Ojha, M. Lee and H. Y. Kim, *Electrochim. Acta*, 2020, **334**, 135537.

34 S. Sun, Y. Sun, Y. Zhou, J. Shen, D. Mandler, R. Neumann and Z. J. Xu, *Chem. Mater.*, 2019, **31**, 8106–8111.

35 Y. Zhang, H. Guo, P. Yuan, K. Pang, B. Cao, X. Wu, L. Zheng and R. Song, *J. Power Sources*, 2019, **442**, 227252.

36 X. Yan, Z. Wang, J. Bao, Y. Song, X. She, J. Yuan, Y. Hua, G. Lv, H. Li and H. Xu, *Nanotechnology*, 2022, **34**, 065401.

37 S. Xu, X. Gao, A. Deshmukh, J. Zhou, N. Chen, W. Peng, Y. Gong, Z. Yao, K. D. Finkelstein and B. Wan, *J. Mater. Chem. A*, 2020, **8**, 2001–2007.

38 K. Min, M. Kim, C. Lim, S. E. Shim, D. Lim and S.-H. Baeck, *Int. J. Hydrogen Energy*, 2021, **46**, 27874–27882.

39 G. Barati Darband, M. Aliofkhazraei, S. Hyun and S. Shanmugam, *ACS Appl. Mater. Interfaces*, 2020, **12**, 53719–53730.

40 S. Xun, Y. Xu, J. He, D. Jiang, R. Yang, D. Li and M. Chen, *J. Alloys Compd.*, 2019, **806**, 1097–1104.

41 V. S. Sapner, P. P. Chavan and B. R. Sathe, *ACS Sustainable Chem. Eng.*, 2020, **8**, 5524–5533.

42 L. Wang, J. Xu, Z. Wang, Z. Wang, Y. Liu, W. Sun, J. Lai, R. Vajtai, P. M. Ajayan and J. M. Tour, *J. Alloys Compd.*, 2020, **843**, 156001.

43 E. Jiang, J. Li, X. Li, A. Ali, G. Wang, S. Ma, P. K. Shen and J. Zhu, *Chem. Eng. J.*, 2022, **431**, 133719.

44 X. Xiong, Y. Ji, M. Xie, C. You, L. Yang, Z. Liu, A. M. Asiri and X. Sun, *Electrochem. Commun.*, 2018, **86**, 161–165.

45 M. K. Bates, Q. Jia, H. Doan, W. Liang and S. Mukerjee, *ACS Catal.*, 2016, **6**, 155–161.

46 D. Li, C. Liu, W. Ma, S. Xu, Y. Lu, W. Wei, J. Zhu and D. Jiang, *Electrochim. Acta*, 2021, **367**, 137492.

47 Y. Yan, H. Liu, C. Liu, Y. Zhao, S. Liu, D. Wang, M. Fritz, A. Ispas, A. Bund and P. Schaaf, *Appl. Mater. Today*, 2021, **25**, 101185.

48 J. Wang, L. Li, L. Wang, Y. Liu, W. Sun, W. Li and G. Li, *ACS Omega*, 2018, **3**, 464–471.

49 L. Tian, H. Chen, X. Lu, D. Liu, W. Cheng, Y. Liu, J. Li and Z. Li, *J. Colloid Interface Sci.*, 2022, **628**, 663–672.

50 I. Ahmad, J. Ahmed, S. Batool, M. N. Zafar, A. Hanif, M. F. Nazar, A. Ul-Hamid, U. Jabeen, A. Dahshan and M. Idrees, *J. Alloys Compd.*, 2022, **894**, 162409.

51 Z. Li, C. Li, J. Huang, W. Sun, W. Cheng, C. He and L. Tian, *Int. J. Hydrogen Energy*, 2022, **47**, 15189–15197.

52 X. Bai, Z. Duan, B. Nan, L. Wang, T. Tang and J. Guan, *Chin. J. Catal.*, 2022, **43**, 2240–2248.

53 X. Gu, Y.-G. Ji, J. Tian, X. Wu and L. Feng, *Chem. Eng. J.*, 2022, **427**, 131576.

54 W. Xie, J. Huang, L. Huang, S. Geng, S. Song, P. Tsiakaras and Y. Wang, *Appl. Catal., B*, 2022, **303**, 120871.

55 Y. Liu, Y. Xing, S. Xu, Y. Lu, S. Sun and D. Jiang, *Chem. Eng. J.*, 2022, **431**, 133240.

56 S. Xiong, L. Wang, H. Chai, Y. Xu, Y. Jiao and J. Chen, *J. Colloid Interface Sci.*, 2022, **606**, 1695–1706.

57 S. Manzoor, A. G. Abid, S. Aman, M. Abdullah, A. R. Rashid, H. M. Ali, T. E. Ali, M. A. Assiri, M. N. Ashiq and T. Taha, *Ceram. Int.*, 2022, **48**, 36975–36982.

58 Y. Mu, Y. Zhang, X. Pei, X. Dong, Z. Kou, M. Cui and C. Meng, *J. Colloid Interface Sci.*, 2022, **611**, 235–245.

59 N. L. W. Septiani, Y. V. Kaneti, K. B. Fathoni, Y. Guo, Y. Ide, B. Yuliarto, X. Jiang, H. K. Dipojono, D. Golberg and Y. Yamauchi, *J. Mater. Chem. A*, 2020, **8**, 3035–3047.

60 H. Chen, G. C. Dismukes and D. A. Case, *J. Phys. Chem. B*, 2018, **122**, 8654–8664.

61 Q. Huo, J. Cao, L. Mi, J. Shao, M. Lv, X. Chen, H. Yang, X. Chai, Q. Hu and C. He, *J. Mater. Chem. A*, 2023, **11**, 1335–1342.

62 W. Li, F. Li, H. Yang, X. Wu, P. Zhang, Y. Shan and L. Sun, *Nat. Commun.*, 2019, **10**, 5074.

63 Y. Liu and C. C. McCrory, *Nat. Commun.*, 2019, **10**, 1683.

64 L. I. Krishtalik, *Biochim. Biophys. Acta, Bioenerg.*, 2000, **1458**, 6–27.

65 M. Suga, F. Akita, M. Sugahara, M. Kubo, Y. Nakajima, T. Nakane, K. Yamashita, Y. Umena, M. Nakabayashi and T. Yamane, *Nature*, 2017, **543**, 131–135.

66 X. Li, F. Pan, C. Sun, M. Zhang, Z. Wang, J. Du, J. Wang, M. Xiao, L. Xue and Z.-G. Zhang, *Nat. Commun.*, 2019, **10**, 519.

67 W. Wang and E. C. Tse, *Inorg. Chem.*, 2021, **60**, 6900–6910.

68 O. V. Boyarkin, M. A. Koshelev, O. Aseev, P. Maksyutenko, T. R. Rizzo, N. F. Zobov, L. Lodi, J. Tennyson and O. L. Polyansky, *Chem. Phys. Lett.*, 2013, **568**, 14–20.

69 T. Liu, G. Li, N. Shen, L. Wang, B. J. Timmer, A. Kravchenko, S. Zhou, Y. Gao, Y. Yang and H. Yang, *Chem. – Eur. J.*, 2022, **28**, e202104562.

70 L. Cao, Q. Luo, J. Chen, L. Wang, Y. Lin, H. Wang, X. Liu, X. Shen, W. Zhang and W. Liu, *Nat. Commun.*, 2019, **10**, 4849.

71 A. Kohen and H.-H. Limbach, *Isotope effects in chemistry and biology*, cRc Press, 2005.

72 K. Schowen, H.-H. Limbach, G. Denisov and R. Schowen, *Biochim. Biophys. Acta, Bioenerg.*, 2000, **1458**, 43–62.

73 C. Costentin, *ACS Catal.*, 2020, **10**, 7958–7967.

74 L. A. Clare, T. D. Pham, L. A. Rafou, A. G. Buenaventura, T. R. Scott, V. Mikhaylova and D. K. Smith, *J. Phys. Chem. C*, 2019, **123**, 23390–23402.

75 L. A. Clare, A. T. Pham, F. Magdaleno, J. Acosta, J. E. Woods, A. L. Cooksy and D. K. Smith, *J. Am. Chem. Soc.*, 2013, **135**, 18930–18941.

76 L. Giordano, B. Han, M. Risch, W. T. Hong, R. R. Rao, K. A. Stoerzinger and Y. Shao-Horn, *Catal. Today*, 2016, **262**, 2–10.